J. Synchrotron Rad. (1999). **6**, 1174–1184

Design and characterization of an undulator beamline optimized for small-angle coherent X-ray scattering at the Advanced Photon Source

A. R. Sandy,[a] L. B. Lurio,[a]* S. G. J. Mochrie,[a] A. Malik,[b] G. B. Stephenson,[b] J. F. Pelletier[c] and M. Sutton[c]

[a]Center for Materials Science and Engineering, Massachusetts Institute of Technology, Cambridge, MA 02139-4307, USA, [b]Materials Science Division, Argonne National Laboratory, Argonne, IL 60439-4832, USA, and [c]Physics Department, McGill University, Montréal, Québec H3A 2T8, Canada. E-mail: larry@slate.imm.aps.anl.gov

(*Received 23 February 1999; accepted 12 July 1999*)

An undulator beamline and small-angle-scattering spectrometer have been implemented at the Advanced Photon Source. The beamline is optimized for performing small-angle wide-bandpass coherent X-ray scattering measurements, and has been characterized by measuring static X-ray speckle patterns from isotropically disordered samples. Statistical analyses of the speckle patterns have been performed from which the speckle widths and contrast are extracted *versus* wavevector transfer and sample thickness. The measured speckle widths and contrast are compared with an approximation to the intensity correlation function and found to be in good agreement with its predictions.

Keywords: coherent X-ray beams; speckle; small-angle X-ray scattering (SAXS).

1. Introduction

Recent experiments have demonstrated the potential of X-ray intensity-fluctuation spectroscopy (XIFS), also known as X-ray photon-correlation spectroscopy (XPCS), to become a powerful probe of sample dynamics at low frequencies ($<10^4$ Hz) and small length scales (<200 nm). For example, XIFS measurements have been made of the equilibrium dynamics of a binary alloy near its critical point (Brauer *et al.*, 1995), of the Brownian motion of gold (Dierker *et al.*, 1995), palladium (Thurn-Albrecht *et al.*, 1996) and antimony oxide (Tsui & Mochrie, 1998), colloids diffusing in glycerol, and of the equilibrium dynamics of block-copolymer micelles in a homopolymer matrix (Mochrie *et al.*, 1997). New insights into non-equilibrium dynamics, such as phase separation in a binary glass (Malik *et al.*, 1998), may also be obtained using this technique. All of these measurements were performed in a regime of wavevector and frequency space which extends beyond what is accessible to various other light, neutron or X-ray scattering techniques (Dierker, 1995).

IFS with laser light has long been employed to investigate the dynamics of condensed matter on micrometre length scales in transparent media. Its principles are well known: a sample is illuminated by coherent laser light, resulting in a random speckle pattern which varies with time as a result of temporal fluctuations within the sample. The time autocorrelation function of the speckle pattern yields the characteristic times of the sample. Key to performing XIFS, therefore, is a sufficiently coherent and intense X-ray beam illuminating the sample under study.

The beam coherence can conveniently be thought of as having two components: (i) transverse or lateral coherence, and (ii) longitudinal or temporal coherence. For a source with an approximately Gaussian intensity distribution, the 'one-sigma' transverse coherence lengths of the beam are given by $\xi = \lambda R/(2\pi\sigma_x)$ in the horizontal direction and $\zeta = \lambda R/(2\pi\sigma_z)$ in the vertical direction, where λ is the X-ray wavelength, R is the source-to-observer distance and σ is the one-sigma source size. The usual transverse coherence lengths, defined by Goodman (1985) in terms of integrals of the source intensity distribution, are related to the one-sigma coherence lengths by $\tilde{\xi} = \pi^{1/2}\xi = \lambda R/(2\pi^{1/2}\sigma_x)$ and $\tilde{\zeta} = \pi^{1/2}\zeta = \lambda R/(2\pi^{1/2}\sigma_z)$. For X-rays produced by undulator A at the Advanced Photon Source (APS), the source sizes are $\sigma_z \simeq 50$ μm in the vertical direction and $\sigma_x \simeq 350$ μm in the horizontal direction so that, for $\lambda \simeq 0.16$ nm and for a sample at $R \simeq 55$ m, the transverse coherence lengths are $\tilde{\zeta} \simeq 50$ μm in the vertical direction and $\tilde{\xi} \simeq 7$ μm in the horizontal direction.

The longitudinal or temporal coherence length of the beam is given by $\Lambda \simeq \lambda(E/\Delta E)$, where E is the energy of the X-ray beam (7.66 keV), ΔE is the full width at half-maximum (FWHM) of the energy spectrum, and the precise numerical factor relating the longitudinal coherence length to the FWHM depends on the energy spectrum

© 1999 International Union of Crystallography
Printed in Great Britain – all rights reserved

(Goodman, 1985). Typically, $\Delta E/E$ takes values of 0.0002 for crystal monochromatization or 0.026 for pink beam. To observe coherent-scattering effects, the optical path difference of the scattered X-rays must not be too much larger than the longitudinal coherence length of the beam. In particular, for a small-angle scattering experiment (wavevector transfers less than approximately 0.2 nm^{-1}), the energy bandwidth for which coherence effects can be observed is relatively large, *i.e.* ~1%. Recent work in this field has exploited this fact (Dierker *et al.*, 1995; Thurn-Albrecht *et al.*, 1996; Tsui & Mochrie, 1998; Mochrie *et al.*, 1997; Tsui *et al.*, 1998; Abernathy *et al.*, 1998; Malik *et al.*, 1998).

Small-angle coherent X-ray scattering experiments are facilitated in two ways at a third-generation undulator-based synchrotron X-ray source. First, the flux of transversely coherent X-rays is directly proportional to the source brilliance. An undulator at the APS therefore routinely provides a factor in excess of 10^4 more transversely coherent X-rays through a unit aperture per unit relative bandwidth than has been available previously at second-generation bending-magnet synchrotron X-ray sources. Second, the energy bandwidth of an undulator harmonic approximately matches the allowed energy bandwidth of the X-ray beam as derived from optical pathlength-difference considerations. Provided that the other undulator harmonics are 'filtered' away, it is then possible to use the entire undulator harmonic for a small-angle coherent-scattering experiment with a concomitant increase in flux.

Motivated by these considerations, we have implemented an X-ray beamline and a spectrometer optimized for performing small-angle wide-bandpass coherent X-ray scattering experiments. We have incorporated several novel features into the design of our apparatus which we describe in detail in §2. §3 outlines the alignment of these various beamline components and our characterization of the radiation source.

A crucial diagnostic for optimizing our beamline for XIFS measurements is a detailed characterization of its performance under static conditions. In particular, we produce static speckle patterns using isotropically disordered aerogels and analyse the scattered intensity using a statistical treatment which is described in detail by Abernathy *et al.* (1998). Our results are compared with a theory developed here. §4 details the results of the statistical analysis of the static speckle patterns and §5 contains a summary and our conclusions.

Table 1
Locations of various key components in our small-angle coherent-scattering set-up.

Item	Distance from source (mm)	Distance from sample (mm)
Undulator A	0	−55000
White-beam slits	27000	−28000
Horizontal-deflection mirror	29200	−25800
Collimating slits	54930	−70
Guard slit	54990	−10
Sample	55000	0
Beam stop	59450	4450
CCD detector	59600	4600

2. Experiment

The scattering measurements described in this paper were carried out at the MIT–McGill–IBM insertion-device beamline at the APS (8-ID). Table 1 lists the distances from the centre of the undulator to various key components, and Fig. 1 is a schematic plan view of the beamline. From right-to-left in Fig. 1, the principal components are as follows.

APS undulator A (Lai *et al.*, 1993; Dejus *et al.*, 1994; Ilinski *et al.*, 1996) is the radiation source. It is a 72-pole 2.4 m-long insertion device located in the downstream half of the sector-8 5 m straight section. The radiation produced by the undulator is peaked at a series of harmonic energies that can be adjusted by changing the gap between the magnet poles. A deflection parameter, K, characterizes the behaviour at a given gap, and is related to the effective magnetic field seen by the particle beam *via* $K = 0.934\ \lambda_u$ [cm] $B_{\rm eff}$ [T]. Here, λ_u is the undulator period and $B_{\rm eff}$ is the effective magnetic field seen by the particle beam. The energy range of the undulator first harmonic spans 3–13 keV (deflection parameter K = 2.57–0.37); we typically operate with the undulator gap set to 18.0 mm, which places the first harmonic at a measured energy of E = 7.66 keV (K = 1.288). The measured FWHM bandwidth for the first undulator harmonic is $\Delta E/E$ = 0.026 FWHM; the source size is σ_x = 350 μm in the horizontal and σ_y = 50 μm in the vertical (Cai *et al.*, 1996). This yields FWHM source sizes of 870 μm × 110 μm in the horizontal and vertical directions, respectively, assuming the source profile is Gaussian. The X-ray beam divergences at 4% coupling are

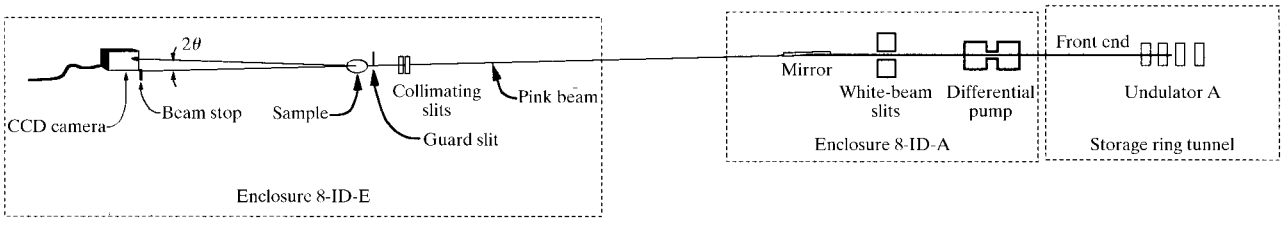

Figure 1
Schematic of the coherent small-angle X-ray scattering beamline and spectrometer.

expected to be $\sigma_{x'}$ = 25 μrad in the horizontal and $\sigma_{y'}$ = 5 μrad in the vertical (Cai *et al.*, 1996).

Radiation propagates from the straight section to our beamline *via* the APS front end (FE) (Kuzay, 1993). The FE connects to our beamline *via* a windowless differential pump. Immediately downstream of the differential pump are white-beam slits. Currently, the maximum aperture of these slits is 275 μm in both the vertical and horizontal directions. This restriction will be waived in the near future. However, the use of such a small aperture limits the heat load on the downstream optics.

The next component is a horizontally deflecting mirror. The mirror is made from a polished single-crystal silicon flat and its glancing incidence angle is 2.6 mrad. The top half of the mirror's optical face is uncoated (Si) and the bottom half is coated with Pt yielding critical energies of 10 keV and 30 keV for reflection from the top and bottom, respectively. Undulator radiation up to the critical energy is reflected from the mirror while higher-energy radiation is absorbed or transmitted through the mirror. Using a mirror as the first optic has several advantages: (i) the heat load on downstream optics is reduced, (ii) the entire undulator spectrum (<30 keV) can be delivered to downstream experiment stations for experiments requiring very high photon fluxes, and (iii) radiation shielding in downstream stations is facilitated. Characterization of the undulator beam reflected from the mirror and delivered downstream to the experiment station (enclosure 8-ID-E) is described in detail in §3.2.

The remaining items in our set-up constitute the small-angle coherent X-ray scattering spectrometer. A pair of crossed slits is used to select a partially transversely coherent portion of the X-ray beam. The slit assembly is a custom design which allows the slit blades to be placed within a few centimetres of the sample and to be entirely contained within a vacuum. The slit blades are made of 2 mm-thick tantalum and their beam-defining edges are rounded and polished to reduce parasitic scattering. The slits have independent adjustable openings in the horizontal and vertical directions from ∼1 μm to 2.5 mm. Independent horizontal and vertical apertures allow us to choose slit openings that best match the different transverse coherence lengths produced by the very different horizontal and vertical source sizes. The resolution and repeatability of the slit blades are ∼0.2 μm and ∼1 μm, respectively.

The samples we studied were contained in a small chamber that is integrated with the incident and exit flight path (no windows). Silica aerogels were used as canonical static speckle-producing samples for the following reasons: (i) they have well characterized scattering over a range of small angles (Sandy *et al.*, 1997); (ii) they scatter strongly; and (iii) they span a variety of thicknesses, which is useful for testing models of speckle.

Immediately upstream of the sample, and inside the sample chamber, is a guard slit made of 3 mm-thick tantalum. Like the slits, its beam-trimming edge was polished. It was used to reduce the parasitic scattering produced by the slits. We used only a single guard slit and mounted it on the inboard (storage-ring) side of the beam with its edge vertical. Likewise, the CCD camera (see below) was mounted so that it only collected scattering in the inboard direction. By working only in the inboard half-plane, we greatly simplified the alignment of the guard slit.

A Princeton Instruments (Princeton Instruments, Trenton, NJ) model EEV-37 thermoelectrically cooled deep-depletion CCD chip with 1152 × 1242 22.5 μm-square pixels directly detected the intensity scattered from the aerogel samples. Its quantum efficiency at the X-ray energy we used was about 20%. Data presented in this paper are the average of between 100 and 200 CCD exposures, each of duration 0.01–1.0 s. Readout time between each of the exposures was 1.5 s. Obtaining data as a time series prevents saturation of the CCD. In addition, it allows the CCD performance to be characterized as described by Dufresne *et al.* (1995).

The CCD was protected from the direct X-ray beam by a beamstop made of tungsten. Both the beamstop and the guard slit are mounted on motorized stages so, by observing in real time the scattered intensity recorded by the CCD, we were able to optimize their positions in order to minimize the parasitic contribution to the measured scattering.

3. Beamline alignment and characterization

3.1. *Alignment*

The alignment or 'steering' of the central cone of the undulator beam with respect to the fixed 3.0 mm-exit-diameter mask that is part of the sector 8 differential pump can be determined by measuring angular profiles of the X-ray beam at fixed energy (Ilinski, 1998). In particular, we note that for detuned energies, E, less than but in the vicinity of an undulator harmonic E_n, the maxima in the angular distribution of the synchrotron radiation appear symmetrically displaced from the centre axis at an angle given approximately by (Ilinski *et al.*, 1996)

$$\theta = \pm (1/\gamma)\left\{0.95\mathcal{E}^2\,[\mathrm{GeV}]\,n/(E\,[\mathrm{keV}]\,\lambda_u\,[\mathrm{cm}]) - \left(1 + K^2/2\right)\right\}^{1/2}, \quad (1)$$

where γ is the particle beam energy, $\mathcal{E}$, divided by its rest mass, λ_u is the period of the undulator, and K is the deflection parameter. At the APS, $\mathcal{E}$ = 7 GeV, λ_u = 3.3 cm and K varies from ∼2.2 to 0.4.

As an example, Fig. 2(*a*) is a profile obtained by scanning a 0.27 mm-diameter pinhole in the vertical direction through the undulator beam and recording the intensity transmitted through it with an Si(111) analyser crystal. The analyser crystal was set so that the accepted energy was E = 7.26 keV; the undulator gap was set so that the first harmonic was peaked at E = 7.66 keV. The measured profile has a local minimum at a vertical pinhole position of ∼0.4 mm and relatively hard cut-offs at ±1.5 mm. The hard cut-offs are the shadow of the 3 mm aperture differential

pump, which limits the size of the X-ray beam accepted by the sector 8 undulator beamline. The local minimum at the detuned energy corresponds to the on-axis position of the undulator at the harmonic energy. These observations allow any necessary beam-steering correction to be easily and reliably determined. For example, in Fig. 2(*a*), the deviation of the central cone from the centre of the fixed 3 mm-diameter aperture is ∼0.4 mm and the 0.27 mm-diameter analysing pinhole is ∼27 m from the source, yielding a steering error of 14 μrad in the vertical direction. A steering correction of 15 μrad down was requested from the APS control room. The result, shown in Fig. 2(*b*), demonstrates that, in the vertical direction at least, the undulator beam is steered correctly into the 3 mm-diameter fixed aperture.

A similar procedure was used to check the X-ray beam steering in the horizontal direction. Now, however, because of the increased emittance of the beam in the horizontal direction, the second harmonic must be used. Fig. 3 is a profile in the horizontal direction of undulator A measured through a 0.27 mm-diameter pinhole and at an energy detuned ∼15% from the peak of the second harmonic. The figure shows that the X-ray beam is correctly steered through the fixed 3 mm-diameter aperture; the 'on-axis' position is the central minimum in the scan. Hard cut-offs at ±1.5 mm are the shadows of the 3 mm-diameter upstream aperture.

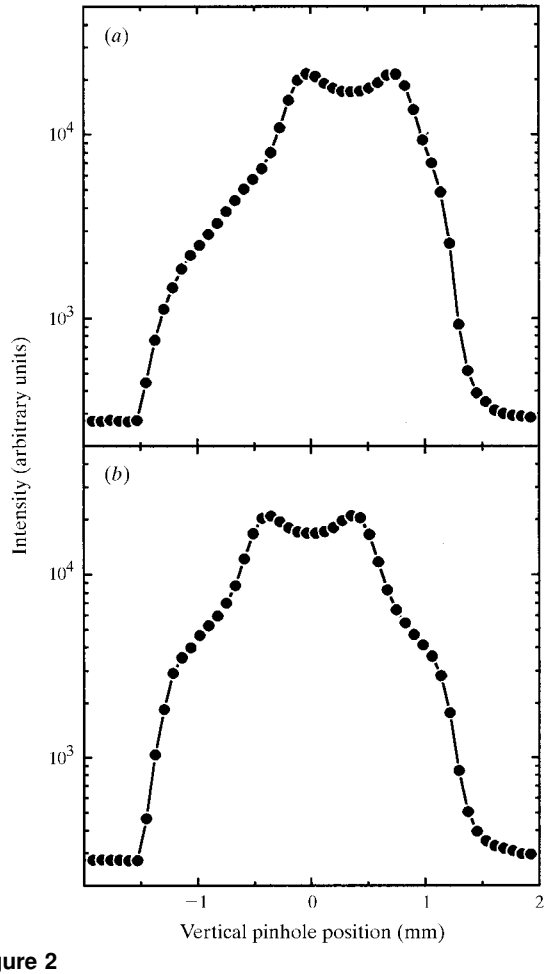

Figure 2
Vertical undulator beam profile measured through a 0.27 mm-diameter pinhole at an energy $E = 7.26$ keV detuned from the first harmonic energy of $E = 7.66$ keV. (*a*) Profile before X-ray-beam steering corrections. The cut-offs at about ±1.5 mm are the shadow of an upstream 3 mm-diameter aperture. (*b*) Profile after a 15 μrad vertical steering correction down. The local minimum in the profile is now centred in the 3 mm-diameter aperture.

3.2. *Undulator characterization*

Fig. 4 shows undulator spectra, for an 18.00 mm undulator gap, plotted on an absolute scale. Solid and dashed lines are measured spectra after reflection from the Si and Pt stripes, respectively, of the mirror – so-called 'pink' beams. (A close-up of the measured first harmonic profile is plotted in Fig. 10.) The dot-dashed line is a calculated spectrum. The measured spectra were obtained by scanning the acceptance energy of an Si(111) analyser-crystal assembly in enclosure 8-ID-E and recording the reflected intensity in a nitrogen-filled ion chamber. The white-beam slits (27.5 m from the source) restricted the accepted beam size to a diameter of 0.27 mm. Glitches in the measured spectra at ∼10, 11.5 and 16 keV are Pt edges and higher-order Si(111) analyser-crystal reflections. The increasing signal at higher energies for the Si-reflected beam is direct-beam scatter entering the ion chamber at small Si(111) analyser-crystal angles. The calculated spectrum was obtained using the program *us* (Dejus & Luccio, 1994) with parameters set to match our beamline configuration. A comparison of the measured and calculated spectrum is given in Table 2.

Evidently, our beamline performs very close to its ideal. For the remaining measurements described in this paper, the mirror was set to reflect from its Si stripe and the undulator gap was set to 18.00 mm ($E_1 = 7.66$ keV). As demonstrated by the solid line in Fig. 4, the mirror then acts

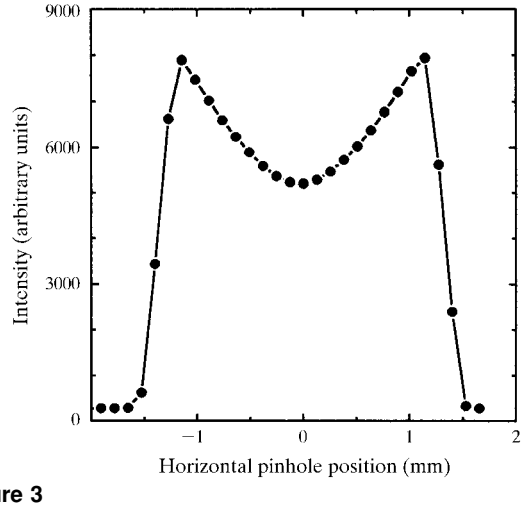

Figure 3
Horizontal undulator beam profile measured through a 0.27 mm-diameter pinhole at an energy $E = 12.6$ keV detuned from the second-harmonic energy of $E = 15.3$ keV. The cut-offs at about ±1.5 mm are the shadow of an upstream 3 mm-diameter aperture.

Table 2
Comparison of measured and calculated parameters for undulator A at 8-ID.

	Measured		Calculated
E_1 (keV)	7.66		7.66
$\Delta E_1/E_1$ (FWHM)	0.026		0.027
	Si	Pt	
I_1^0 [photons s^{-1} (100 mA)$^{-1}$ (0.1% bandwidth)$^{-1}$]	3×10^{13}	2×10^{13}	3×10^{13}
I_1^{int} [photons s^{-1} (100 mA)$^{-1}$]	1.1×10^{15}	7×10^{14}	1.1×10^{15}

as a low-pass filter with a roll-off energy just above the first harmonic; the entire undulator first harmonic is delivered to the experiment with minimal higher-order harmonic contamination.

3.3. *Source-size characterization*

We have found that a straightforward means to measure the effective undulator beam source size is as follows. [More precise measurements are described by Cai *et al.* (1996)]. The white-beam slits are approximately equidistant from the centre of the 8-ID undulator (the source) and our experiment apparatus (~27.5 m). If the white-beam slits are made very small they effectively function as a pinhole camera for imaging the source. Fits to the derivatives of the profiles obtained by scanning a 'knife-edge' across the beam in the horizontal and vertical directions at the experiment position then yield the effective source sizes without any further deconvolution.

Fig. 5 illustrates this idea. Open circles are the numerical derivative of the profile obtained by scanning a single blade of a slit vertically across the X-ray beam at the sample position in the experiment enclosure at sector 8. The inset to Fig. 5 is the original profile. The vertical gap of the white-beam slits was set to 30 μm for these measurements. Fits by Gaussian profiles to the peak and the trough in the data (solid line) yield a one-sigma source size in the vertical of 60 μm. A similar procedure for a scan in the horizontal (with the white-beam slits defining an aperture of 120 μm in the horizontal) yields a one-sigma source size in the horizontal of 330 μm. These results are in good agreement with the more careful measurements of Cai *et al.* (1996) which yielded one-sigma source sizes of 50 μm and 350 μm in the vertical and horizontal directions, respectively.

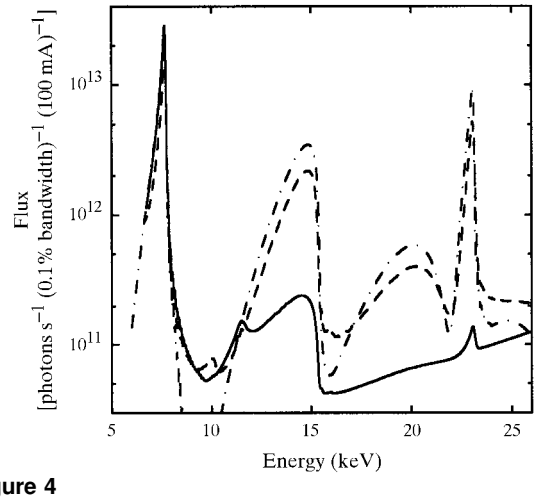

Figure 4
APS undulator A spectra with the undulator gap set to 18.00 mm. The solid line is the measured spectrum after reflection from the Si portion of the mirror, the dashed line is the measured spectrum reflected from the Pt-coated portion of the mirror, and the dot-dashed line is the predicted white-beam spectrum. The measured full-width-at-half-maximum energy bandwidth of the first harmonic is $\Delta E/E = 0.026$.

4. Results and discussion

Fig. 6 shows the small-angle scattering produced by (*a*) 7 μm × 21 μm (H × V) and (*b*) 15 μm × 31 μm partially coherent X-ray beams incident upon a 1.2 mm-thick aerogel and (*c*) a 6 μm × 21 μm partially coherent X-ray beam incident upon a 2.7 mm-thick aerogel. Typical flux through the slits was of the order of 10^{12} photons s^{-1} and scaled with the aperture area. The white-beam slits, which can produce an effectively smaller source size if partially closed (see later), were open for all three sets of these measurements so that the transverse coherence lengths of the X-ray beam are determined by the source-to-sample distance, the source sizes and the collimating-slit apertures. For all the images presented in Fig. 6, dark regions indicate more recorded scattering and light regions indicate less. The bottom panels are the entire range of scattering that

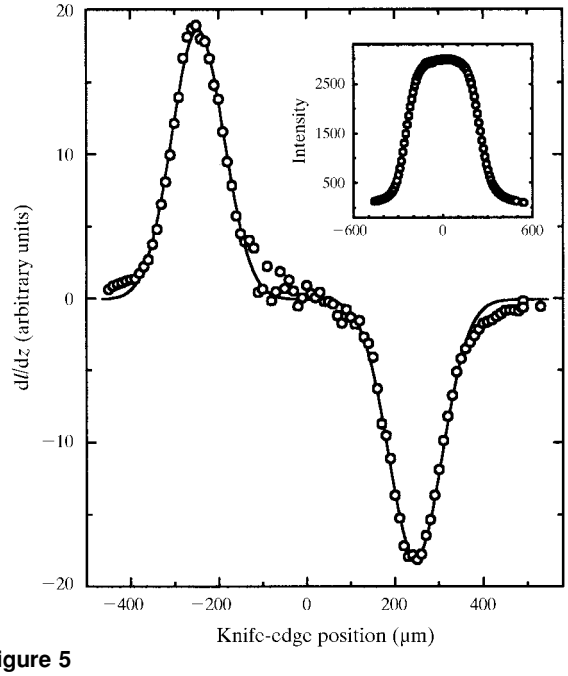

Figure 5
Numerical derivative of a 'knife-edge' scanned vertically across the X-ray beam. The knife-edge is 28 m downstream of a pinhole; the pinhole is 27 m downstream of the source. The solid line is a fit by two Gaussian profiles. The inset is the original scan.

was collected while the top panels are close-ups in the range of **Q** indicated. Each image is the average of 100 CCD exposures (frames). The exposure time per frame for (*a*) was 0.1 s, for (*b*) 0.03 s, and for (*c*) 0.05 s. All the data presented in Fig. 6 have been converted to wavevector transfer (**Q**) using the relation $\mathbf{Q} = k\mathbf{r}/R_d$, where $k = 2\pi/\lambda = 38.8\ \mathrm{nm}^{-1}$ is the wave number, **r** is a vector from a point on the CCD image plane to the beam-zero position on the CCD image plane, and R_d is the separation between the sample and the detector (see Table 1). The direct beam (stopped by a beam stop) is at $|\mathbf{Q}| = Q = 0$, Q_x is in the horizontal direction and Q_z is in the vertical direction.

There are several notable qualitative features apparent in Fig. 6. First, for all three patterns the measured scattering is grainy – this is speckle! Second, for all three patterns the speckles appear streaked in the radial direction. This is on account of the non-zero energy bandwidth of the X-ray beam. Third, we observe that for increased sample thickness the longitudinal widths of the speckles decreases. This is especially apparent when we compare the speckle-pattern close-up for the 1.2 mm-thick aerogel [top panel of Fig. 6(*a*)] with the speckle-pattern close-up for the 2.7 mm-thick aerogel [top panel of Fig. 6(*c*)]. Finally, the 15 μm × 31 μm beam incident upon a given sample produces many more speckles compared with the 7 μm × 21 μm beam [compare the bottom panels of Figs. 6(*a*) and 6(*b*)]. This observation is quite consistent with the smaller speckle size expected for larger slit settings.

In order to quantify these observations, we now turn to a statistical analysis of the static X-ray speckle patterns. We omit detailed explanations of this formalism as it has recently been presented by Abernathy *et al.* (1998). A similar analysis was also recently given by Tsui *et al.* (1998).

First, the detector response is characterized by calculating the spatial autocorrelation of each CCD frame in a region where the measured intensity is very weak (isolated photon 'hits') (Dufresne *et al.*, 1995), in order to determine the spatial resolution of the detector independent of complicating intensity variations due to the speckle pattern itself. From this analysis we find that the FWHM detector resolution is 2.0 pixels or $3.8 \times 10^{-4}\ \mathrm{nm}^{-1}$ in both the vertical and horizontal directions.

Key to the remainder of the analysis is the two-point intensity correlation function,

$$C(\mathbf{r}_1, \mathbf{r}_2) = \langle I(\mathbf{r}_1) I(\mathbf{r}_2) \rangle / \langle I(\mathbf{r}_1) \rangle \langle I(\mathbf{r}_2) \rangle, \qquad (2)$$

where r_i are points in the CCD image plane, and the angle brackets indicate a spatial average over a suitable region of the time average of a series of CCD frames. The spatial autocorrelation function is maximized for $\mathbf{r}_1 = \mathbf{r}_2$ [$1 < C(\mathbf{r},\mathbf{r}) \leq 2$], while for large separations it decays to 1. The contrast of the speckle pattern – an important figure-of-merit for a

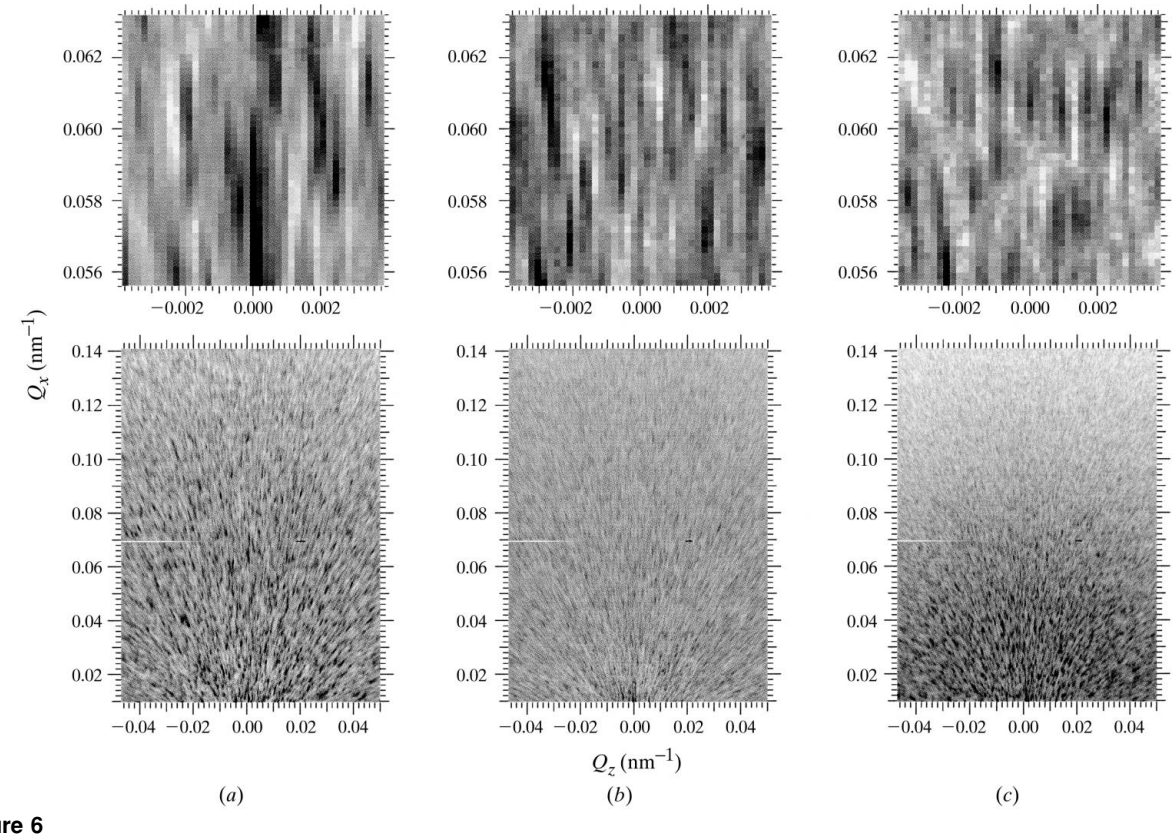

Figure 6
Speckle patterns produced by a wide-bandpass partially coherent X-ray beam incident upon aerogel samples. Scattering produced by (*a*) 7 μm × 21 μm (H × V) beam incident upon a 1.2 mm-thick aerogel sample. (*b*) 15 μm × 31 μm beam incident upon a 1.2 mm-thick aerogel sample. (*c*) 6 μm × 21 μm beam incident upon a 2.7 mm-thick aerogel sample. The bottom panel of each pair of figures is the entire range of scattering collected; the top panel is a close-up in the range of **Q** indicated.

scattering experiment with partially coherent X-rays – is the background-subtracted value of the maximum of the spatial autocorrelation function, $\beta(\mathbf{r}) = C(\mathbf{r},\mathbf{r}) - 1$, and consequently takes on values $[0 \leq \beta(\mathbf{r}) \leq 1]$. The FWHMs of the background-subtracted intensity-correlation function, $C(\mathbf{r}_1,\mathbf{r}_2) - 1$, yield the speckle widths. As an example, Fig. 7 shows the intensity autocorrelation at $Q \cong 0.060$ nm^{-1} calculated for the speckle pattern produced by 1.2 mm-thick aerogel illuminated by a 7 μm × 21 μm (H × V) partially coherent X-ray beam [top panel of Fig. 6(*a*)]. Open circles are data in the longitudinal direction and solid circles are data in the transverse direction. Evidently the speckles are considerably broader in the longitudinal direction than in the transverse direction. This feature is also obvious from inspection of the top panel of Fig. 6(*a*).

The results from analysing those portions of the three speckle patterns in Fig. 6 that lie within a region bounded by lines extending from the origin at ±15° from the vertical are plotted in Figs. 8 and 9. Plotted symbols in Fig. 8 are the experimentally determined contrasts *versus* wavevector transfer for the three different sets of sample and X-ray beam parameters described above. Specifically, open circles are the measured contrast for the 7 μm × 21 μm (H × V) X-ray beam incident upon the 1.2 mm-thick aerogel, open squares are the measured contrast for the 15 μm × 31 μm X-ray beam incident upon the 1.2 mm-thick aerogel, and open triangles are the measured contrast for the 6 μm × 21 μm X-ray beam incident upon the 2.7 mm-thick aerogel. For all three sets of measurements, the measured contrast decreases continuously with increasing wavevector transfer. Moreover, for the same collimating slit setting, we see that the measured contrast decreases with increasing sample thickness. Lastly, we see that, especially for increasing wavevector transfer, the contrast from a sample of given thickness decreases with increasing collimating slit aperture.

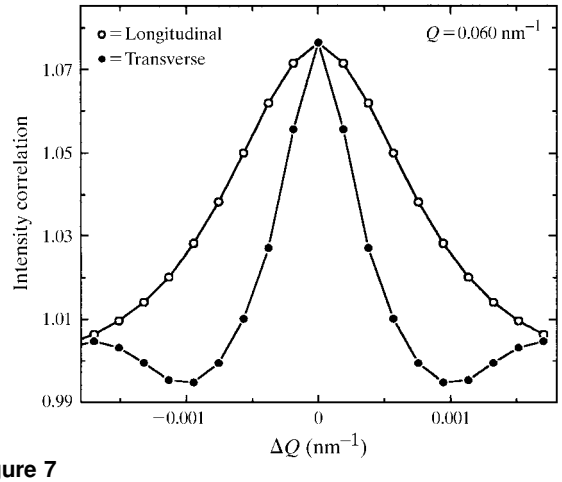

Figure 7
Intensity autocorrelation in the radial (open circles) and transverse (solid circles) directions for the speckle pattern described in the text. The separation between points corresponds to the size of pixels on the CCD. Solid lines are guides-to-the-eye.

Open and solid plotted symbols in Fig. 9 are the experimentally determined speckle widths *versus* wavevector transfer in the radial and transverse directions, respectively, for the three different sets of sample and X-ray beam parameters described above. Specifically, open circles are the measured radial speckle widths for the 7 μm × 21 μm (H × V) X-ray beam incident upon the 1.2 mm-thick aerogel, open squares are for the 15 μm × 31 μm X-ray beam incident upon the 1.2 mm-thick aerogel, and open triangles are for the 6 μm × 21 μm X-ray beam incident upon the 2.7 mm-thick aerogel. The same sequence of symbols but now solid apply for the transverse speckle widths. As anticipated previously, the transverse speckle widths are considerably less than the radial speckle widths. Moreover, the transverse speckle widths appear to be independent of wavevector transfer while the radial speckle widths do not.

There are several approaches available for predicting the contrast and speckle widths of speckle patterns as a function of wavevector transfer, sample thickness and so forth (Abernathy *et al.*, 1998; Tsui *et al.*, 1998; Sinha *et al.*, 1998). An approximation that we have found effective and will further elaborate here has been given by Pusey (1976). He derives that in the Fraunhofer limit the contrast of a speckle pattern is given by

$$\beta = \int_V d^3\mathbf{r}_1 \int_V d^3\mathbf{r}_2 \times \left|\left\langle E(\mathbf{0},0)E^*\left(\mathbf{r}_2^{\perp} - \mathbf{r}_1^{\perp}, \mathbf{Q}\cdot\left[\mathbf{r}_2 - \mathbf{r}_1\right]/ck\right)\right\rangle\right|^2 / V^2\left\langle |E|^2\right\rangle^2, \quad (3)$$

where $E(\mathbf{r}, t)$ is the incident electric field at position $\mathbf{r}$ and time t, $\mathbf{Q}$ is the scattering vector, k is the wave number and c is the speed of light. [$\mathbf{r}^{\perp} = (x, 0, z)$ is the component of $\mathbf{r}$

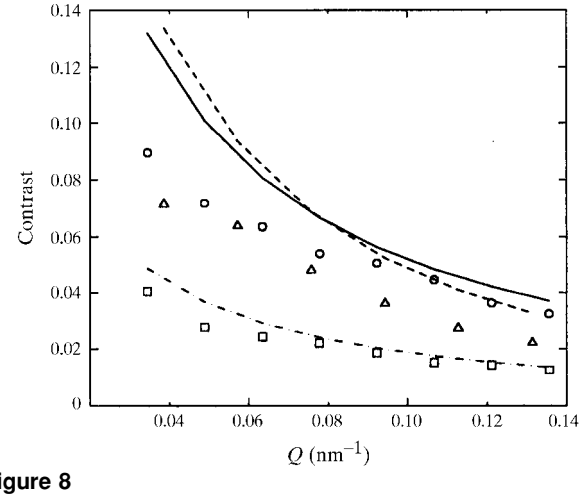

Figure 8
Measured (plotted symbols) and predicted (lines) speckle contrast *versus* wavevector transfer. Open circles and the solid line are results for a 1.2 mm-thick aerogel illuminated by a 7 μm × 21 μm (H × V) beam, open squares and the dot-dashed line are results for a 1.2 mm-thick aerogel illuminated by a 15 μm × 31 μm beam, and open triangles and the dashed line are results for a 2.7 mm-thick aerogel illuminated by a 6 μm × 21 μm beam.

perpendicular to the incident X-ray wavevector.] The integration volume, V, is the illuminated sample volume, which we take to be a solid rectangle of dimensions L along x (x is horizontal and orthogonal to the incident X-ray wavevector), M along z (z is vertical) and W along y. The incident wavevector is $\mathbf{k}_i = (0, k, 0)$ and the scattered wavevector is $\mathbf{k}_f = k(\sin 2\theta \cos\varphi, \cos 2\theta, \sin 2\theta \sin\varphi)$. The wavevector transfer is therefore $\mathbf{Q} = 2k \sin\theta(\cos\theta \cos\varphi, \sin\theta, \cos\theta \sin\varphi)$.

Equation (3) assumes that the correlation length of density (dielectric constant) fluctuations in the sample is much less than the sample dimensions and the transverse and longitudinal coherence lengths of the incident radiation. It also assumes that the coherence time of the incident electric field is much less than the correlation time of the sample. Both of these assumptions are valid for our measurements.

Further assuming, first, that the coherence properties of the radiation can indeed be factored into independent spatial and temporal parts [*i.e.* that the radiation exhibits 'cross-spectral purity' (Born & Wolf, 1980)], second, that the source is incoherent and shows a Gaussian intensity distribution, and, third, that the power spectrum of the radiation is Lorentzian, giving rise to an exponential time correlation function, then the electric field correlation function in (3) can be written as

$$\begin{aligned}\left|\left\langle E(\mathbf{0},0)E^*\left(\mathbf{r}_2^\perp - \mathbf{r}_1^\perp, \mathbf{Q}\cdot\left[\mathbf{r}_2 - \mathbf{r}_1\right]/ck\right)\right\rangle\right| / \left\langle |E|^2\right\rangle \\ = \exp\left[-(x_2 - x_1)^2/2\xi^2\right] \exp\left[-(z_2 - z_1)^2/2\zeta^2\right] \\ \times \exp[-|\delta|/\Lambda],\end{aligned} \tag{4}$$

where Λ is the longitudinal coherence length, and

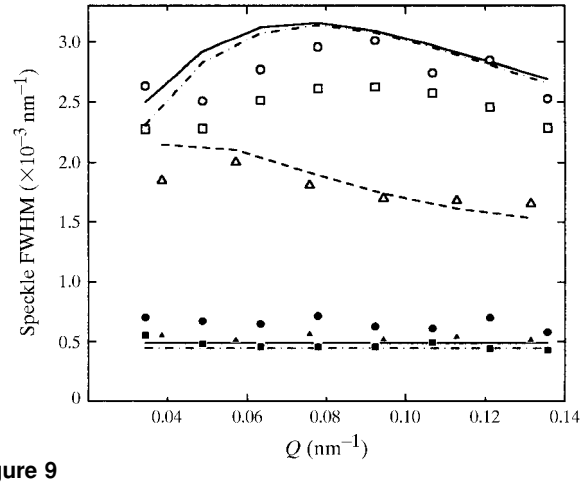

Figure 9
Measured (plotted symbols) and predicted (lines) speckle widths in the radial and transverse directions *versus* wavevector transfer. Open and closed symbols are measured radial and transverse widths, respectively. Open and solid circles are results for a 1.2 mm-thick aerogel illuminated by a 7 μm × 21 μm (H × V) beam, open and solid squares are results for a 1.2 mm-thick aerogel illuminated by a 15 μm × 31 μm beam, and open and solid triangles are results for a 2.7 mm-thick aerogel illuminated by a 6 μm × 21 μm beam. The lines are described in the text.

$$\begin{aligned}\delta = {} & 2\sin\theta\cos\theta\cos\varphi(x_2 - x_1) \\ & + 2\sin^2\theta(y_2 - y_1) \\ & + 2\sin\theta\cos\theta\sin\varphi(z_2 - z_1)\end{aligned} \tag{5}$$

is the optical path difference between two points within the sample at $\mathbf{r}_1 = (x_1, y_1, z_1)$ and $\mathbf{r}_2 = (x_2, y_2, z_2)$.

With regard to the longitudinal coherence, the power spectrum of the electric field fluctuations corresponding to an exponential correlation function with correlation time τ is

$$S(\nu) = 2\tau/\left\{1 + [2\pi\tau(\nu - \nu_0)]^2\right\}. \tag{6}$$

The FWHM of the power spectrum is $1/(\pi\tau)$. It follows for a Lorentzian spectrum that the longitudinal coherence length is $\Lambda = c\tau = (k\Delta\lambda/2\lambda)^{-1}$, where c is the speed of light, *i.e.* $\Lambda = (\lambda/\pi)(E/\Delta E)$, where ΔE is the FWHM of the energy spectrum of the undulator. In fact, the undulator spectrum in the vicinity of the first harmonic is not a Lorentzian; we discuss below why this approximation seems to work well.

To make comparisons with our experimental measurements, we must determine how the coherence lengths are related to the source sizes (σ_x, σ_z), the X-ray wavelength (λ) and the source-to-sample distance (R). For an incoherent source with a Gaussian intensity distribution, the van Cittert–Zernicke theorem (Born & Wolf, 1980) tells us that the spatial part of the electric field correlation function appearing in equation (4) is given by

$$\begin{aligned}\left|\left\langle E(\mathbf{0},0)E^*\left(\mathbf{r}_2^\perp - \mathbf{r}_1^\perp, 0\right)\right\rangle\right| / \left\langle |E|^2\right\rangle \\ = (1/2\pi\sigma_x\sigma_y) \\ \times \int_{-\infty}^{\infty} \mathrm{d}u \exp[-u^2/2\sigma_x^2 + 2\pi i u(x_2 - x_1)/R\lambda] \\ \times \int_{-\infty}^{\infty} \mathrm{d}v \exp[-u^2/2\sigma_y^2 + 2\pi i v(y_2 - y_1)/R\lambda] \\ = \exp[-2\pi^2\sigma_x^2(x_2 - x_1)^2/(\lambda R)^2] \\ \times \exp[-2\pi^2\sigma_y^2(z_2 - z_1)^2/(\lambda R)^2].\end{aligned} \tag{7}$$

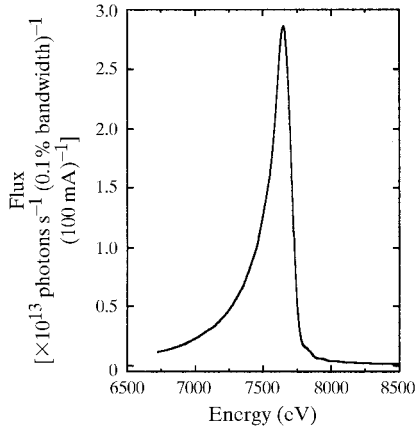

Figure 10
Measured energy spectrum of undulator A in the vicinity of the first harmonic with the undulator gap set to 18.00 mm.

Comparing equations (4) and (7) shows that the one-sigma coherence lengths are related to the one-sigma undulator A source sizes by $\xi = \lambda R/2\pi\sigma_x \simeq 4$ μm and $\zeta = \lambda R/2\pi\sigma_z \simeq 28$ μm.

To derive the contrast from equation (3), we use the sample and beam dimensions described above. We also assume that the sample is immediately adjacent to the collimating slits (in the 'near-field') or, more quantitatively, that $\lambda D/d < d$, where D is the slit-to-sample distance ($\sim$7 cm) and d is the slit aperture. This condition is satisfied for both our horizontal and vertical slits. At zero azimuth ($\varphi = 0$), the six-dimensional integral in equation (3) factors into the product of a four-dimensional integral involving x_1, x_2, y_1 and y_2 (β_r) and a two-dimensional integral involving z_1 and z_2 (β_z). Strictly, our statistical analysis calculates the speckle contrast and widths averaged within a range of $\pm 15^\circ$ about zero azimuth. However, we believe that the speckle widths and contrast calculated for $\varphi = 0$ should be a good approximation to this average and, for calculational convenience, we make this approximation.

The integral over z_1 and z_2 is

$$\begin{aligned}\beta_z &= (1/M^2)\int_0^M \mathrm{d}z_1 \int_0^M \mathrm{d}z_2\, \exp[-(z_2 - z_1)^2/\zeta^2] \\ &= (2/M^2)\int_0^M \mathrm{d}z\,(M - z)\exp(-z^2/\zeta^2) \\ &= (\zeta^2/M^2)\big[(M/\zeta)\pi^{1/2}\,\mathrm{erf}(M/\zeta) + \exp(-M^2/\zeta^2) - 1\big],\end{aligned} \tag{8}$$

where erf() is the error function.

The integral over x_1, x_2, y_1 and y_2 is

$$\begin{aligned}\beta_r = (1/L^2W^2)&\int_0^{LL}\mathrm{d}x_1\,\mathrm{d}x_2 \int_0^{WW}\mathrm{d}y_1\mathrm{d}y_2 \\ &\times \exp[-(x_2 - x_1)^2/\xi^2 - |A(x_2 - x_1) + B(y_2 - y_1)|],\end{aligned} \tag{9}$$

where $A = 4\sin\theta\cos\theta/\Lambda = 4k(\Delta\lambda/\lambda)\sin\theta\cos\theta = 2(\Delta\lambda/\lambda)Q(1 - Q^2/4k^2)^{1/2}$, and $B = 4\sin^2\theta/\Lambda = (\Delta\lambda/\lambda)(Q^2/k)$. Making use of the transformations given by Welling & Griffin (1982), the four-dimensional integral for β_r may be transformed into a two-dimensional integral,

$$\begin{aligned}\beta_r = (2/L^2W^2)&\int_0^L \mathrm{d}x\,(L - x)\int_0^W \mathrm{d}y\,(W - y)\exp(-x^2/\xi^2) \\ &\times[\exp(-|Ax + By|) + \exp(-|Ax - By|)],\end{aligned} \tag{10}$$

which may be evaluated numerically. The final result, therefore, for the contrast is

$$\beta = \beta_r\beta_z. \tag{11}$$

By generalizing Pusey's discussion, it is possible to calculate how the intensity scattered at a wavevector $\mathbf{Q}$ is correlated with the intensity at a different wavevector $\mathbf{Q}' = \mathbf{Q} + \boldsymbol{\kappa}$. Equation (2.37) in Pusey (1976) should be rewritten with the exponential factor replaced by $\exp(-i\mathbf{Q}'[\mathbf{r}_1 - \mathbf{r}_2] - i\mathbf{Q}\cdot[\mathbf{r}_3 - \mathbf{r}_4])$. An additional factor $\exp(-i\kappa\cdot[\mathbf{r}_1 - \mathbf{r}_2])$ then appears in the second factorial moment of the intensity. We may therefore introduce the second factorial moments as a function of κ,

$$\beta(\kappa) = \beta_r(\kappa_x, \kappa_y)\beta_z(\kappa_z), \tag{12}$$

where

$$\begin{aligned}\beta_r(\kappa_x, \kappa_y) = (2/L^2W^2)&\int_0^L \mathrm{d}x\,(L - x)\int_0^W \mathrm{d}y\,(W - y) \\ &\times \exp(-x^2/\xi^2)\big[\exp(-|Ax + By|) \\ &\times \cos(\kappa_x x + \kappa_y y) \\ &+ \exp(-|Ax - By|)\cos(\kappa_x x - \kappa_y y)\big],\end{aligned} \tag{13}$$

and

$$\beta_z(\kappa_z) = (2/M^2)\int_0^M \mathrm{d}z\,(M - z)\exp(-z^2/\zeta^2)\cos(\kappa_z z). \tag{14}$$

Equations (13) and (14) characterize the average speckle shape in three-dimensional reciprocal space. The corresponding speckle widths (Δ_x, Δ_y and Δ_z) are derived by numerical evaluation of (13) and (14). A CCD camera makes a particular cut through reciprocal space, such that the wavevector difference between pixels corresponding to different scattering angles at fixed azimuth (κ_r) and the wavevector difference corresponding to the same scattering angle at different azimuths (κ_t) are related to κ_x, κ_y and κ_z *via*

$$\begin{aligned}\kappa_x &= \cos 2\theta\cos\varphi\kappa_r - \sin\varphi\kappa_t \\ \kappa_y &= \sin 2\theta\kappa_r \\ \kappa_z &= \cos 2\theta\sin\varphi\kappa_r + \cos\varphi\kappa_t.\end{aligned} \tag{15}$$

It should be noted that $\beta_r = \beta_r(\kappa_r)$ and $\beta_z = \beta_z(\kappa_t)$. Equation (15) at $\varphi = 0$ in conjunction with (13) and (14) may be used to calculate the perfectly resolved widths of the autocorrelations in the radial and tangential directions (Δ_r and Δ_t, respectively).

Finally, in order to compare the predictions with our experimentally measured speckle widths and contrast, we must include in the model the smearing produced by the detector resolution. Following the approach described by Abernathy *et al.* (1998), we obtain

$$\beta = \beta_r\beta_z = \frac{\beta_r^0\Delta_r^0}{\big[(\Delta_r^0)^2 + \Delta_d^2\big]^{1/2}}\frac{\beta_z^0\Delta_z^0}{\Big[\big(\Delta_z^0\big)^2 + \Delta_d^2\Big]^{1/2}}, \tag{16}$$

$$\Delta_r = \Big[\big(\Delta_r^0\big)^2 + \Delta_d^2\Big]^{1/2} \tag{17}$$

and

$$\Delta_z = \Big[\big(\Delta_z^0\big)^2 + \Delta_d^2\Big]^{1/2}. \tag{18}$$

The superscripts '0' denote the perfectly resolved widths and contrasts derived above [equations (11), (13) and (14)], Δ_d is the detector resolution = 2 pixels = 3.80×10^{-4} nm^{-1}.

Before making detailed comparisons with our measurements, we note a few general features and simplifications of

the model. First, speckle widths in the z (transverse) direction are predicted to be independent of X-ray beam bandwidth, wavevector transfer and sample thickness. Our speckle-width data (Fig. 9) are consistent with the latter two observations (the bandwidth prediction was not tested). Second, the equation [equation (9)] for the perfectly resolved radial contribution to the contrast simplifies considerably in the limit of small wave vectors and/or vanishing relative bandwidth. Specifically, we find

$$\beta_r = (2/L^2)\int_0^L \mathrm{d}x\,(L-z)\exp(-x^2/\xi^2)$$
$$= (\xi^2/L^2)\big[(L/\xi)\pi^{1/2}\,\mathrm{erf}(L/\xi) + \exp(-L^2/\xi^2) - 1\big],$$

which is the same as equation (8). In these limits and when $L \gg \xi$, then $\beta_r \cong \pi^{1/2}\xi/L$. Similarly, for $M \gg \zeta$, $\beta_z \cong \pi^{1/2}\zeta/M$. Therefore, in these limits,

$$\beta \cong \tilde{\xi}\tilde{\zeta}/(LM), \tag{19}$$

i.e. the coherence area divided by the illuminated sample area.

Solid, dot-dashed and dashed lines in Fig. 8 are the model predictions for the contrast for the experiment conditions corresponding to the plotted open circles, the open squares and the open triangles, respectively. The model predicts the correct wavevector dependence for the contrast and evidently also predicts the correct trends in the contrast as the sample thickness is varied and the slit sizes are changed. It does an adequate job of predicting the overall value of the contrast but the measured values of the contrast are systematically less than the predicted values. Possibly the discrepancy arises because the recorded scattering is contaminated by a small incoherent background arising from the slits and the beamline windows (Abernathy *et al.*, 1998). In fact, Abernathy *et al.* (1998) propose that the beam incident upon the sample can be thought of as being composed of a coherent fraction (α) and an incoherent fraction ($1 - \alpha$). They then show that the expected contrast needs to be scaled by α^2. In the context of this idea, we therefore see that the beam delivered to the sample has a coherent fraction of at least 0.8 over the entire range of measured wavevector transfers. Alternatively, the discrepancy may originate in the azimuthal averaging over $\pm 15^\circ$ that is not accounted for in our calculation.

Now we consider the speckle widths. Lines plotted in Fig. 9 are the model's predictions for the speckle widths for the various experiment conditions corresponding to the plotted symbols. Near the top of the figure, the solid, dot-dashed and dashed lines are the predicted radial speckle widths *versus* wavevector transfers for a 1.2 mm-thick sample illuminated by a 7 μm × 21 μm (H × V) partially coherent X-ray beam, a 1.2 mm-thick sample illuminated by a 15 μm × 31 μm beam, and a 2.7 mm-thick sample illuminated by a 6 μm × 21 μm beam, respectively. The model evidently predicts the correct trends as the sample thickness, slit aperture and wavevector transfer are varied. Moreover, the predicted values of the radial speckle widths are in reasonable agreement with the measured values.

The variation of the longitudinal speckle width *versus* wavevector transfer for a particular sample thickness can be intuitively understood by considering the two contributions to the effective slit size *versus* Q as seen at the detector. The first effect is the foreshortening of the slit aperture with increasing scattering angle which leads to a quadratic increase in the longitudinal speckle width with increasing Q. The second effect results from the increase in the apparent sample thickness with increasing Q. The effective sample thickness is proportional to an effective slit width which leads to a $1/Q$-dependence for the speckle width *versus* increasing Q. The first effect dominates at small Q and the second at larger Q leading to the maximum observed in all three radial speckle-width curves plotted in Fig. 9. We also note that the first effect is independent of the sample thickness while the second is not and predicts that thicker samples yield narrower speckles. In this way we can understand the overall decrease in the longitudinal speckle widths with increasing sample thickness which is also observed in Fig. 9.

Near the bottom of Fig. 9 the solid line is the predicted transverse speckle width for a sample (of arbitrary thickness) illuminated by a 6 or 7 μm × 21 μm (H × V) partially coherent X-ray beam and the dot-dashed line is the prediction for a sample illuminated by a 15 μm × 31 μm beam. The predicted transverse speckle widths are independent of Q and sample thickness and, for the range of vertical slit openings plotted in Fig. 9, dominated by the resolution of the CCD detector (0.38×10^{-3} nm^{-1}). The predicted transverse speckle widths are in good agreement with the measured speckle widths.

Before concluding we wish to further comment on our use of a Lorentzian to approximate the power spectrum of the undulator harmonic [see the discussion of equation (6) above] and why it seems to produce results in agreement with our measurements. Goodman (1985) has given a general expression for the longitudinal coherence length,

$$\Lambda = c\tilde{\tau} = c\int_{-\infty}^{\infty} \mathrm{d}t\,|\langle E(0)E^*(t)\rangle|^2/|\langle E(0)E^*(0)\rangle|^2. \tag{20}$$

It then follows from Parseval's theorem that the longitudinal coherence length is related to the power spectrum *via*

$$\Lambda = c\int_{-\infty}^{\infty} \mathrm{d}\nu\,S(\nu)^2. \tag{21}$$

The measured energy spectrum of undulator A (plotted on an absolute scale) in the vicinity of the first harmonic is shown in Fig. 10. White-beam slits (27.5 m from the source) restricted the accepted beam size to a diameter of 0.27 mm. We may determine Λ for the 'pink-beam' spectrum produced at 8-ID by numerically evaluating (21). Specifically, we have calculated

$$\Lambda = hc \int_{-\infty}^{\infty} \mathrm{d}E\, S(E)^2 \Big/ \left[\int_{-\infty}^{\infty} \mathrm{d}E\, S(E)\right]^2, \qquad (22)$$

where $S(E)$ is now the unnormalized spectrum shown in Fig. 10 (truncated at $E = 8500$ eV) and h is Planck's constant. The result is that $\Lambda = 1/(0.013k)$, which is indistinguishable from $\Lambda = (\lambda/\pi)(E/\Delta E)$ obtained for the Lorentzian distribution. It is this coincidence that renders a Lorentzian spectrum a good approximation.

5. Conclusions

We have implemented a beamline and a spectrometer optimized for performing small-angle coherent X-ray scattering experiments. A horizontally deflecting mirror is used to isolate the first harmonic of the undulator from the 'white' incident spectrum and produce a 'pink' beam incident upon the small-angle coherent-scattering spectrometer. The spectrometer illuminates the sample under study with a partially coherent X-ray beam and records the scattered intensity *via* an area detector.

We have used this set-up to measure static speckle patterns from isotropically disordered samples under a variety of conditions. The static speckle patterns have been analysed using a statistical approach from which we obtain the speckle widths and contrast *versus* wavevector transfer. The results have been compared with an approximation, described in detail, to the intensity correlation function. We find that the predicted speckle contrast and widths agree very well with the observed values. We conclude that our set-up is performing at close to its optimum level. Nevertheless, it should be noted that the speckle contrast is quite low ($\sim$0.05). In principle, it would be possible to improve the speckle constrast by a factor of ten by reducing the bandwidth by a factor of ten, which would be valuable for XIFS experiments on radiation-sensitive samples, reducing by tenfold the total flux on the sample, while leaving the coherent flux unchanged. In practice, however, monochromators yielding a relative bandwidth of $\sim$0.003 FWHM are not readily available at present.

We thank Douglas Abernathy and Gerhard Grübel of the European Synchrotron Radiation Facility, Peter Ilinski of the APS, and Matt Borthwick, Peter, Falus and Dirk Lumma of MIT for illuminating conversations. We appreciate Norbert Mulders of the University of Delaware for supplying the aerogel samples used in this work. We are especially grateful to Douglas Abernathy for providing many of the 'Yorick' routines that were used as the basis for the speckle analysis presented here. We also acknowledge the expert technical assistance of Harold Gibson. This work was supported by NSF grant DMR-9312543 and DOE BES grant DE-FG02-96ER45593 to MIT, the ANL LDRD program and NSERC. Use of the APS was supported by the US DOE (BES, OER) under Contract No. W-31-109-Eng-38.

References

Abernathy, D. L., Grübel, G., Brauer, S., McNulty, I., Stephenson, G. B., Mochrie, S. G. J., Sandy, A. R., Mulders, N. & Sutton, M. (1998). *J. Synchrotron Rad.* **5**, 37–47.

Born, M. & Wolf, E. (1980). *Principles of Optics.* Oxford: Pergamon Press.

Brauer, S., Stephenson, G. B., Sutton, M., Brüning, R., Dufresne, E., Mochrie, S. G. J., Als-Nielsen, J., Grübel, G. & Abernathy, D. L. (1995). *Phys. Rev. Lett.* **74**, 2010–2013.

Cai, Z., Dejus, R. J., Den Hartog, P., Feng, Y., Gluskin, E., Haeffner, D., Ilinski, P., Lai, B., Legnini, D., Moog, E. R., Shastri, S., Trakhtenberg, E., Vasserman, I. & Yun, W. (1996). *Rev. Sci. Instrum.* **67**, 3348.

Dejus, R. J., Lai, B., Moog, E. R. & Gluskin, E. (1994). *Undulator A Characteristics and Specifications: Enhanced Capabilities.* Technical Report ANL/APS/TB-17. Argonne National Laboratory, Argonne, IL 60439-4832, USA.

Dejus, R. J. & Luccio, A. (1994). *Nucl. Instrum. Methods*, A**347**, 61–66.

Dierker, S. B. (1995). *X-ray Photon Correlation Spectroscopy at the NSLS.* NSLS Newsletter. NSLS, Upton, NY, USA.

Dierker, S. B., Pindak, R., Fleming, R. M., Robinson, I. K. & Berman, L. (1995). *Phys. Rev. Lett.* **75**, 449–452.

Dufresne, E., Brüning, R., Sutton, M., Rodricks, B. & Stephenson, G. B. (1995). *Nucl. Instrum. Methods*, A**364**, 380–393.

Goodman, J. W. (1985). *Statistical Optics.* New York: John Wiley & Sons.

Ilinski, P. (1998). *Undulator A Diagnostics at the Advanced Photon Source.* Technical Report ANL/APS/TB-33. Argonne National Laboratory, Argonne, IL 60439-4832, USA.

Ilinski, P., Dejus, R. J., Gluskin, E. & Morrison, T. I. (1996). *Optics for High-Brightness Synchrotron Radiation Beamlines II*, Vol. 2856, edited by L. E. Berman & J. R. Arthur, pp. 16–25. Washington: SPIE.

Kuzay, T. (1993). *Functional Description of APS Beamline Front Ends.* Technical Report ANL/APS/TB-5. Argonne National Laboratory, Argonne, IL 60439-4832, USA.

Lai, B., Khounsary, A., Savoy, R., Moog, L. & Gluskin, E. (1993). *Undulator A Characteristics and Specifications.* Technical Report ANL/APS/TB-3. Argonne National Laboratory, Argonne, IL 60439-4832, USA.

Malik, A., Sandy, A. R., Lurio, L. B., Stephenson, G. B., Mochrie, S. G. J., McNulty, I. & Sutton, M. (1998). *Phys. Rev. Lett.* **81**, 5832–5835.

Mochrie, S. G. J., Mayes, A. M., Sandy, A. R., Sutton, M., Brauer, S., Stephenson, G. B., Abernathy, D. L. & Grübel, G. (1997). *Phys. Rev. Lett.* **78**, 1275–1278.

Pusey, P. N. (1976). *Photon Correlation Spectroscopy and Velocimetry*, edited by H. Z. Cummins & E. R. Pike, pp. 45–141. New York: Plenum.

Sandy, A. R., Lurio, L. B., Mochrie, S. G. J., Malik, A., Stephenson, G. B. & Sutton, M. (1997). *Coherent Electron-Beam X-ray Sources: Techniques and Applications*, Vol. 3154, edited by A. K. Freund, H. P. Freund & M. R. Howells, pp. 27–38. Washington: SPIE.

Sinha, S. K., Tolan, M. & Gibaud, A. (1998). *Phys. Rev. B*, **57**, 2740–2758.

Thurn-Albrecht, T., Steffen, W., Patkowski, A., Meier, G., Fischer, E. W., Grübel, G. & Abernathy, D. L. (1996). *Phys. Rev. Lett.* **77**, 5437–5440.

Tsui, O. K. C. & Mochrie, S. G. J. (1998). *Phys. Rev. E*, **57**, 2030–2034.

Tsui, O. K. C., Mochrie, S. G. J. & Berman, L. E. (1998). *J. Synchrotron Rad.* **5**, 30–36.

Welling, F. & Griffin, A. (1982). *Phys. Rev. B*, **25**, 2450–2462.